

Simulations of nanosecond-pulsed dielectric barrier discharges in atmospheric pressure air

Cite as: J. Appl. Phys. **113**, 113301 (2013); <https://doi.org/10.1063/1.4795269>

Submitted: 29 January 2013 . Accepted: 28 February 2013 . Published Online: 15 March 2013

Moon Soo Bak, and Mark A. Cappelli



View Online



Export Citation



CrossMark

ARTICLES YOU MAY BE INTERESTED IN

[Modeling and simulation of plasma gas flow driven by a single nanosecond-pulsed dielectric barrier discharge](#)

Physics of Plasmas **23**, 103510 (2016); <https://doi.org/10.1063/1.4964727>

[Numerical simulation of nanosecond pulsed dielectric barrier discharge actuator in a quiescent flow](#)

Physics of Fluids **26**, 036102 (2014); <https://doi.org/10.1063/1.4867708>

[On the quenching of excited electronic states of molecular nitrogen in nanosecond pulsed discharges in atmospheric pressure air](#)

Applied Physics Letters **98**, 011502 (2011); <https://doi.org/10.1063/1.3535986>



Your Qubits. Measured.

Meet the next generation of quantum analyzers

- Readout for up to 64 qubits
- Operation at up to 8.5 GHz, mixer-calibration-free
- Signal optimization with minimal latency

Find out more



Simulations of nanosecond-pulsed dielectric barrier discharges in atmospheric pressure air

Moon Soo Bak and Mark A. Cappelli

Mechanical Engineering Department, Stanford University, Stanford, California 94305, USA

(Received 29 January 2013; accepted 28 February 2013; published online 15 March 2013)

This paper describes simulations of nanosecond pulse plasma formation between planer electrodes covered by dielectric barriers in air at atmospheric pressure and 340 K. The plasma formation process starts as electrons detach from negative ions of molecular oxygen that are produced from the previous discharge pulse. An ionization front is found to form close to the positively biased electrode and then strengthens and propagates towards the grounded electrode with increasing gap voltage. Charge accumulation and secondary emission from the grounded electrode eventually lead to sheath collapse. One interesting feature is a predicted reversal in gap potential due to the accumulated charge, even when there is no reversal in applied potential. The simulation results are compared to recent measurement of mid-gap electric field under the same discharge conditions [Ito *et al.*, *Phys. Rev. Lett.* **107**, 065002 (2011)]. © 2013 American Institute of Physics.
[\[http://dx.doi.org/10.1063/1.4795269\]](http://dx.doi.org/10.1063/1.4795269)

I. INTRODUCTION

Repetitively pulsed nanosecond discharges produce non-equilibrium plasmas of relatively high peak and average electron number densities with lower overall power budgets when compared to direct-current thermal plasmas.¹ The higher electron (and ion) densities and ensuing chemical reactivity make these discharges of interest to applications such as plasma-assisted combustion^{2,3} and plasma-driven flow actuation.^{4,5} The formulation of kinetic mechanisms in these discharges has been based almost exclusively on a combination of optical emission spectroscopy and kinetics simulations.^{6–8} A few simulation studies^{9–11} have been conducted for this type of discharge, coupling the discharge kinetics to discharge dynamics which describe the time-evolution of the electric field, and electron and ion drifts, particularly in plane-to-plane configurations in which dielectric barriers are imposed between the electrodes and the bulk plasma. However, these simulations are either in relatively low pressures of tens of Torr or at relatively high temperatures of a few thousand Kelvin. In this paper, simulations have been carried out at the condition of high pressure (atmospheric pressure) and cold temperature (340 K) where average and peak discharge electron densities are several orders of magnitude higher even in glow mode than those from the referred studies above and therefore the plasma is more susceptible to a glow-to-arc transition. These so-called dielectric barrier discharge (DBD) configurations are relevant in applications of these nanosecond pulsed discharges to plasma-assisted aerodynamics.^{4,5,12,13}

Although spatially and temporally resolved emission has been measured in nanosecond pulsed discharges of varying electrode configurations and operating conditions,^{6,7,14} the measurement of other discharge properties such as plasma density or electric field is scarce. Recently, Ito *et al.*¹⁴ reported on spatially and time-resolved measurements of the electric field within the gap of a nanosecond-pulsed plane-to-plane DBD in 300 K atmospheric pressure air and with a

1.15 mm electrode spacing. They found that space-charge development within the gap forms within a few nanoseconds suggesting that strong ionization is preceded by a significant charge accumulation on the dielectric barriers associated with the drifting charges present prior to the application of the voltage pulse. It seems therefore that the relatively high pulse repetition rate (10 kHz) does not allow for the plasma to fully recombine, resulting in a discharge dynamic that is strongly affected by the presence of charges from the previous pulse.

In this paper, we report on the development of a one-dimensional simulation of nanosecond-pulsed planar dielectric barrier discharges to investigate the structure and dynamics of discharges similar to those studied experimentally in Ref. 14. The simulations presented here are carried out for conditions similar to those presented in Ref. 14, with planar electrodes covered by 0.15 mm thick glass plates (dielectric constant of 4.6) and separated by 1.15 mm (gap of 0.85 mm), as schematically illustrated in Fig. 1. The simulated discharge is in atmospheric pressure air at a temperature of 340 K, consistent with the reported gas temperature measured in the experiment.¹⁴ At this time, we simulate a single pulse only and account for the repetitive nature of the discharge through initial conditions on the gas temperature (340 K) and charged species density carried over from the previous discharge pulse.

II. SIMULATION DETAILS

The simulations are carried out with the upper electrode in Fig. 1 at ground potential and with the voltage pulse applied to the bottom electrode (referred to here as the “driven electrode”). The temporal shape of the voltage applied in the simulations and that measured at the driven electrode by Ito *et al.*¹⁴ are shown in the inset of Fig. 1. The voltage is bipolar, with the pulse shapes resembling slightly skewed-Gaussian distributions in time (FWHM of 15 ns), peaking first at a positive value of about 4.5 kV followed by the negatively biased pulse peaking at 2.5 kV about 30 ns later. As a result, the

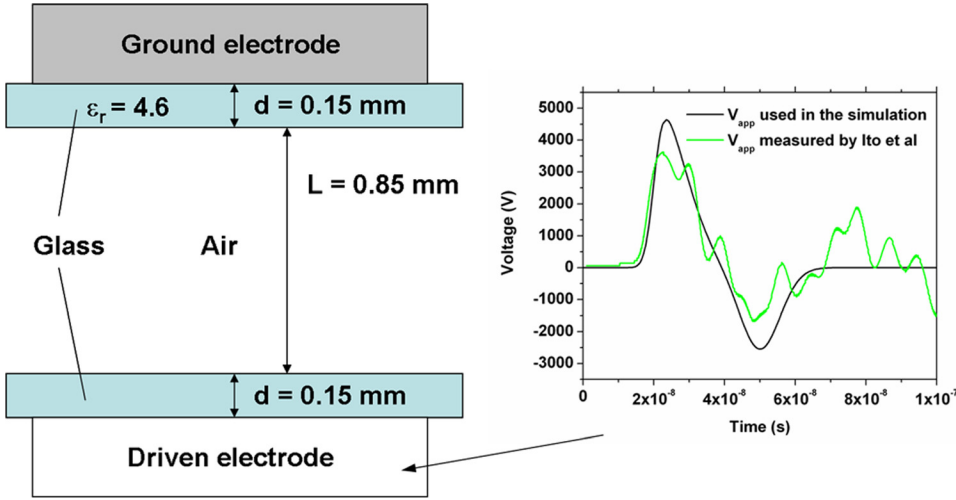


FIG. 1. Simulation schematic (left frame) and plot of applied voltage variation in time to the driven electrode (right frame). Also shown in the plot is the voltage measured on the driven electrode by Ito *et al.*¹⁴

driven electrode first serves as an anode, but actually completing the discharge as a cathode. As shown below, this complex pulse shape has significant consequence on the discharge dynamics.

The simulations are performed on a uniform grid with a grid cell size of $3.4 \mu\text{m}$. The electron/ions number density,

electron energy, and electric potential (voltage) are computed at the cell center, whereas the electric field is computed at the cell boundaries. The system of equations includes the continuity equations for the densities of the electrons, positive ions (N_2^+ and O_2^+), negative ions (O_2^-), and the excited electronic species ($\text{N}_2 \text{ C}$)

$$\frac{\partial n_e}{\partial t} + \frac{\partial \Gamma_e}{\partial x} = \left[k_{\text{ioniz}, \text{N}_2} n_e n_{\text{N}_2} + k_{\text{ioniz}, \text{O}_2} n_e n_{\text{O}_2} + k_{\text{detach}} n_{\text{O}_2^-} n_{\text{total}} - k_{\text{attach}} n_e n_{\text{O}_2} - k_{\text{attach}, 3} n_e n_{\text{O}_2} n_{\text{total}} \right] - k_{\text{recomb}} n_{\text{N}_2^+} n_e - k_{\text{recomb}} n_{\text{O}_2^+} n_e, \quad (1)$$

$$\frac{\partial n_{\text{N}_2^+}}{\partial t} + \frac{\partial \Gamma_{\text{N}_2^+}}{\partial x} = [k_{\text{ioniz}, \text{N}_2} n_e n_{\text{N}_2} - k_{\text{recomb}} n_{\text{N}_2^+} n_e - k_{\text{recomb}, \text{ions}} n_{\text{N}_2^+} n_{\text{O}_2^-} - k_{\text{conv}, \text{ions}} n_{\text{N}_2^+} n_{\text{O}_2}], \quad (2)$$

$$\frac{\partial n_{\text{O}_2^+}}{\partial t} + \frac{\partial \Gamma_{\text{O}_2^+}}{\partial x} = [k_{\text{ioniz}, \text{O}_2} n_e n_{\text{O}_2} - k_{\text{recomb}} n_{\text{O}_2^+} n_e - k_{\text{recomb}, \text{ions}} n_{\text{O}_2^+} n_{\text{O}_2^-} + k_{\text{conv}, \text{ions}} n_{\text{N}_2^+} n_{\text{O}_2}], \quad (3)$$

$$\frac{\partial n_{\text{O}_2^-}}{\partial t} + \frac{\partial \Gamma_{\text{O}_2^-}}{\partial x} = [k_{\text{attach}} n_e n_{\text{O}_2} + k_{\text{attach}, 3} n_e n_{\text{O}_2} n_{\text{total}} - k_{\text{detach}} n_{\text{O}_2^-} n_{\text{total}} - k_{\text{recomb}, \text{ions}} (n_{\text{O}_2^+} + n_{\text{N}_2^+}) n_{\text{O}_2^-}], \quad (4)$$

$$\frac{\partial n_*}{\partial t} + \frac{\partial \Gamma_*}{\partial x} = [k_{\text{excit}} n_e n_{\text{N}_2} - k_{\text{quen}} n_* n_{\text{total}} - \nu_{\text{quen}} n_*], \quad (5)$$

together with the electron energy equation and the equations for the surface charge densities, σ , at the dielectric surfaces (separated by the spacing, L)

$$\frac{\partial}{\partial t} \left(\frac{3}{2} n_e k T_e \right) + \frac{\partial q_e}{\partial x} = -e \Gamma_e E - \sum_{j=\text{inelastic collisions}} H_j R_j, \quad (6)$$

$$\frac{d\sigma_{\text{dielec}, \text{ground electrode}}}{dt} = -e (\Gamma_{\text{N}_2^+}(0) + \Gamma_{\text{O}_2^+}(0) - \Gamma_e(0) - \Gamma_{\text{O}_2^-}(0)), \quad (7)$$

$$\frac{d\sigma_{\text{dielec}, \text{driven electrode}}}{dt} = e (\Gamma_{\text{N}_2^+}(L) + \Gamma_{\text{O}_2^+}(L) - \Gamma_e(L) - \Gamma_{\text{O}_2^-}(L)). \quad (8)$$

These equations are solved simultaneously with an implicit numerical scheme. The drift-diffusion approximation is assumed for the electrons and ions

$$\Gamma_e = -D_e \frac{\partial n_e}{\partial x} - \mu_e n_e E, \quad (9)$$

$$\Gamma_{\text{N}_2^+} = -D_{\text{N}_2^+} \frac{\partial n_{\text{N}_2^+}}{\partial x} + \mu_{\text{N}_2^+} n_{\text{N}_2^+} E, \quad (10)$$

$$\Gamma_{O_2^+} = -D_{O_2^+} \frac{\partial n_{O_2^+}}{\partial x} + \mu_{O_2^+} n_{O_2^+} E, \quad (11)$$

$$\Gamma_{O_2^-} = -D_{O_2^-} \frac{\partial n_{O_2^-}}{\partial x} - \mu_{O_2^-} n_{O_2^-} E, \quad (12)$$

$$\Gamma_* = -D_* \frac{\partial n_*}{\partial x}. \quad (13)$$

In the above equations, n_j is the number density of species j , Γ_j is the corresponding flux, E is the electric field, D_j is the diffusion coefficient, and μ_j is the species mobility. The diffusion coefficient is related to the mobility through the Einstein relation

$$D_j = \frac{\mu_j k T_j}{e}. \quad (14)$$

For ions, the temperature is assumed to be equal to that of the neutral species temperature. The electron heat flux and thermal conductivity are formulated as

$$q_e = -K_e \frac{\partial T_e}{\partial x} + \frac{5}{2} k T_e \Gamma_e, \quad (15)$$

$$K_e = \frac{3}{2} k D_e n_e. \quad (16)$$

Here, k is the Boltzmann constant and T_e is the electron temperature. In the energy equation, R_j is rate of j -th electron inelastic collisions (here, we consider only N_2 and O_2 as collision partners for these inelastic collisions), and H_j is the associated energy loss per electron. The reader can find the complete list of inelastic electron scattering data for collisions with N_2 and O_2 from Refs. 15 and 16. This last term in the energy equation therefore accounts for the electron energy loss by all inelastic collisions, which result in rotational, vibrational, electronic excitations, as well as the ionizations of N_2 and O_2 .

The mobility of positive and negative ions is taken from Ref. 17

$$\mu_i = 2100/p_{[\text{Torr}]}, \text{ cm}^2/(\text{V} \cdot \text{s}) \quad E/p < 49.3 \text{ V}/(\text{cm} \cdot \text{Torr}),$$

$$\mu_i = (14750/p_{[\text{Torr}]}) \sqrt{E/p_{[\text{Torr}]}} \text{ cm}^2/(\text{V} \cdot \text{s})$$

$$E/p > 49.3 \text{ V}/(\text{cm} \cdot \text{Torr}).$$

The kinetic mechanism and corresponding reaction rate coefficients, k_s used in the above equations are summarized in Table I. In this table, k_{ioniz,N_2} and k_{ioniz,O_2} are the electron-impact ionization rate coefficients of N_2 and O_2 , respectively. The electron detachment, binary, and three-body electron attachment rate coefficients are k_{detach} , k_{attach} , and $k_{\text{attach},3}$, respectively. The rate coefficients for recombination between either the electrons and ions, or positive and negative ions are k_{recomb} and $k_{\text{recomb,ions}}$. The ion conversion rate coefficient resulting from collisions between N_2^+ and O_2 is

$k_{\text{conv,ions}}$, the electron-impact excitation rate coefficient of the N_2 (C) state is k_{excit} , and k_{quen} and ν_{quen} are the collisional and radiation quenching rate coefficients of N_2 (C). Calculations of D_e , μ_e , and the reaction rate coefficients involving electrons are facilitated using the commercially available BOLSIG⁺ software package.¹⁸ In carrying out the simulations, D_e and μ_e are pre-tabulated as a function of reduced electric field (Td) and the rate coefficients are pre-tabulated as a function of mean electron energy (eV).

A total current density, J_{total} , is computed by adding a displacement current density, $J_{\text{displacement}}$, to a net charge conduction current density, $J_{\text{conduction}}$

$$J_{\text{conduction}} = e(\Gamma_{N_2^+} + \Gamma_{O_2^+} - \Gamma_e - \Gamma_{O_2^-}),$$

$$J_{\text{displacement}} = \epsilon_0 \frac{\partial E}{\partial t}, \quad (17)$$

$$J_{\text{total}} = J_{\text{conduction}} + J_{\text{displacement}}.$$

The electric field at the cell boundaries is updated after each time step by solving Poisson's equation with boundary conditions imposed by surface charges on the dielectric barriers

$$\frac{\partial}{\partial x}(\epsilon_0 E) = e(n_{N_2^+} + n_{O_2^+} - n_e - n_{O_2^-})$$

$$+ \sigma_{\text{dielec, ground electrode}} \delta(x)$$

$$+ \sigma_{\text{dielec, driven electrode}} \delta(x - L), \quad (18)$$

$$-(\epsilon_r \epsilon_0) E_{\text{dielec, ground electrode}} + \epsilon_0 E_{\text{gas, ground electrode}}$$

$$= \sigma_{\text{ground electrode}}$$

$$-\epsilon_0 E_{\text{gas, driven electrode}} + (\epsilon_r \epsilon_0) E_{\text{dielec, driven electrode}}$$

$$= \sigma_{\text{driven electrode}}, \quad (19)$$

$$-E_{\text{dielec, ground electrode}} d$$

$$- \int_0^L E dx - E_{\text{dielec, driven electrode}} d = V_{\text{app}}(t). \quad (20)$$

Here, δ is the Dirac-delta function and ϵ_0 and ϵ_r represent the permittivity of vacuum and the relative permittivity of the glass, respectively. In Eqs. (19) and (20), $E_{\text{dielec, ground electrode}}$ and $E_{\text{dielec, driven electrode}}$ are the electric fields inside the grounded electrode- and driven electrode-side dielectric barriers, whereas $E_{\text{gas, ground electrode}}$ and $E_{\text{gas, driven electrode}}$ are the electric fields at the dielectric barrier surfaces of grounded electrode and driven electrode, respectively. The dielectric barrier thickness is d and the applied voltage is V_{app} . Finally, secondary electron emission induced by positive ion bombardment at the dielectric barrier surface provides a boundary condition on the electron flux

$$\Gamma_e = -\gamma \Gamma_+. \quad (21)$$

In the simulations, the secondary electron emission coefficient, γ , is set to be 0.01, and the secondary electrons are assumed to have the energy of 1 eV. The results were found to be somewhat insensitive to the assumed emitted electron

TABLE I. Reactions and the rate coefficients.

Reactions	Rate coefficient	References
$N_2 + e \rightarrow N_2^+ + 2e$	$k_{\text{ioniz},N_2}(\sigma) \text{ m}^3/\text{s}$	15
$O_2 + e \rightarrow O_2^+ + 2e$	$k_{\text{ioniz},O_2}(\sigma) \text{ m}^3/\text{s}$	16
$O_2^- + M \rightarrow O_2 + M + e$, $M = N_2, O_2$	$k_{\text{detach}} = 2 \times 10^{-16} \exp(-0.52/T_{\text{ef2}})[1 - \exp(-4\theta)]/[1 - \exp(-\theta)] \text{ m}^3/\text{s}$ $\theta = 0.13(T^{-1} - T_{\text{ef2}}^{-1})$, $T_{\text{ef2}} = T + 5.2 \times 10^{-6}(E/n)^2$ where T and T_{ef2} are in eV, and E/n is in Td.	24 ^a
$e + O_2 + M \rightarrow O_2^- + M$, $M = N_2, O_2$	$k_{\text{attach},3} = 1.07 \times 10^{-43}(300/T_e)^2 \exp(-70/T) \exp(1500 \times (T_e - T)/T_e/T) \text{ m}^6/\text{s}$ if $M = N_2$ $k_{\text{attach},3} = 1.4 \times 10^{-41}(300/T_e) \exp(-600/T) \exp(700 \times (T_e - T)/T_e/T) \text{ m}^6/\text{s}$ if $M = O_2$	25
$e + M^+ \rightarrow M$, $M = N_2, O_2$	$k_{\text{recomb}} = 2.0 \times 10^{-13}(300/T_e)^{0.5} \text{ m}^3/\text{s}$	25
$M^+ + O_2^- \rightarrow M + O_2$, $M = N_2, O_2$	$k_{\text{recomb,ions}} = 2.0 \times 10^{-13}(300/T)^{0.5}[1 + 10^{-24}n_{\text{total}}(300/T)^2] \text{ m}^3/\text{s}$	25
$N_2^+ + O_2 \rightarrow N_2 + O_2^+$	$k_{\text{ion,conv}} = 6.0 \times 10^{-17}(300/T)^{0.5} \text{ m}^3/\text{s}$	26
$e + N_2(X) \rightarrow e + N_2(C)$	$k_{\text{excit}}(\sigma) \text{ m}^3/\text{s}$	15
$N_2(C) + M \rightarrow N_2(X) + M$	$k_{\text{quen}} = 10^{-17} \text{ m}^3/\text{s}$ if $M = N_2$ $k_{\text{quen}} = 3 \times 10^{-16} \text{ m}^3/\text{s}$ if $M = O_2$	26
$N_2(C) \rightarrow N_2(X)$	$\nu_{\text{quen}} = 3 \times 10^7 \text{ s}^{-1}$	26

^aThe detachment rate coefficient of $M = N_2$ is estimated from that of $M = O_2$.

temperature since within the adjacent sheath region the electrons are expected to gain an amount of energy that greatly exceeds the assumed initial value. However, the results are sensitive to the assumed secondary electron emission coefficient.

For initial conditions, we assume uniform negative and positive ion densities across the domain. The initial densities are estimated to be 10^{16} m^{-3} based on a peak value for the plasma density of 10^{19} m^{-3} and a three-body ion-ion recombination rate coefficient of about $10^{-12} \text{ m}^3/\text{s}$ at 1 atm and 300 K.¹⁹ Since electrons preferentially attach to molecular oxygen when the electric field is weak and the ion conversion time between N_2^+ and O_2 is shorter than the pulse repetition time, we assume that the fate of all remaining electrons is to form O_2^- and all positive ions is O_2^+ . The simulations were carried out to the next pulse to verify the self consistency of these initial conditions.

The equations are discretized according to the Scharfetter-Gummel scheme,²⁰ which affords improved numerical stability when solving drift-diffusion problems. The system of equations (less Poisson's equation) is solved iteratively with an adaptive time step using the SUNDIAL package.²¹ Poisson's equation is solved by the method of lower-upper (LU) triangular matrix decomposition using the linear algebra package (LAPACK).²²

III. RESULTS

The spatial-temporal distributions of electric potential (voltage), electric field, and electron density are shown in the color maps of Figs. 2(a), 3, and 4, respectively. The electric potentials at the driven electrode, grounded electrode (flat-line, zero potential), and both dielectric surfaces are shown in Fig. 2(b). Since the electrons have a generally higher drift velocity than the ions, once generated, their dynamics tend to dominate in determining the discharge structure and characteristics, particularly over time scales comparable to the discharge pulse width. As the voltage applied to the driven electrode increases up to about 2.2 kV (corresponding to a nominal electric field, defined as the applied voltage divided

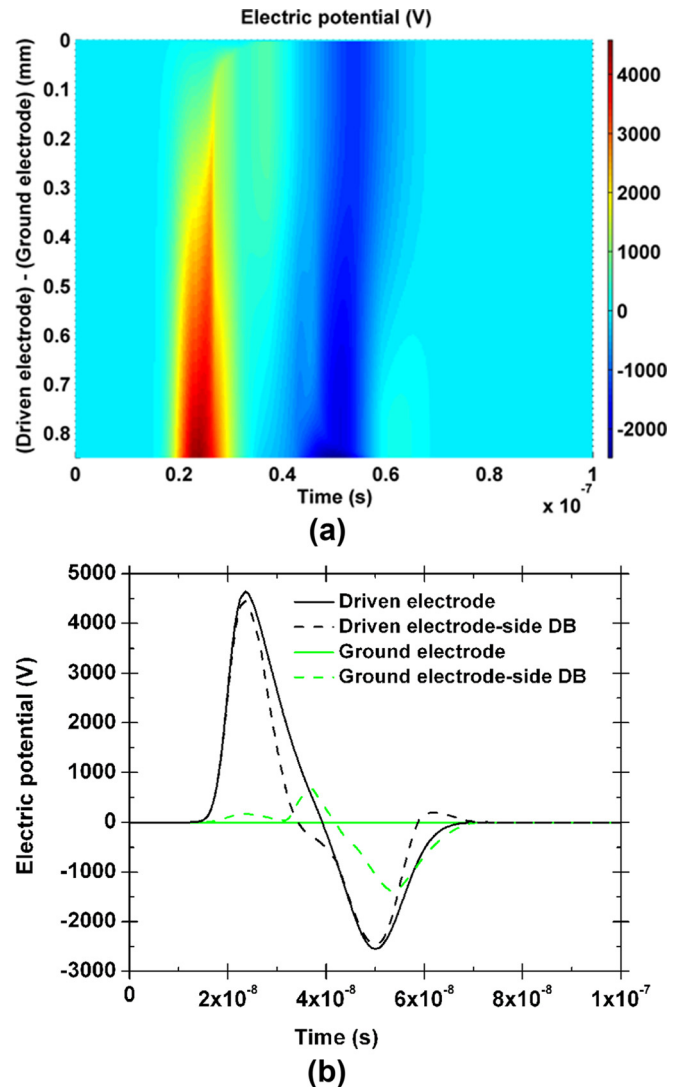


FIG. 2. (a) Spatial-temporal distribution of electric potential (voltage), and (b) temporal electric potentials at both ground and driven electrodes and also the dielectric barrier surfaces.

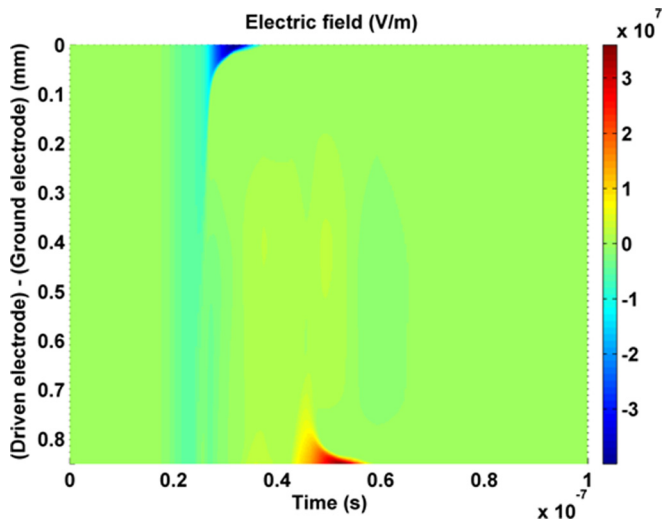


FIG. 3. Spatial-temporal distribution of the electric field.

by the gap spacing, $E = 2.6 \times 10^6$ V/m, or a reduced nominal field of $E/n = 120$ Td, negative and positive ions begin to drift towards the driven and grounded electrodes, respectively; however, the electric field does not depart significantly from the nominal field, little or no charge develops on the dielectric barriers, and the potential at the barrier surfaces is close to nominal values (see Fig. 2(b) up to 19.5 ns) because the initial densities are low, electrons are still bound to molecular oxygen, and ions do not move very far during this time. As the potential increases further, at approximately 22 ns, electrons are detached from O_2^- ions and ionization begins across the domain. The electrons produced by this ionization drift and diffuse towards the positively biased driven electrode and positive ions are left behind; however, these ions are not sufficient to shield the applied potential. Gaining energy from the field, these electrons result in further ionization, producing positive ions which accumulate some distance from the grounded electrode. Once the ion density reaches a critical level (known as the Meek's criterion²³), a rapid strengthening of this ionization front occurs (from 25.5 ns to 26.5 ns) as it

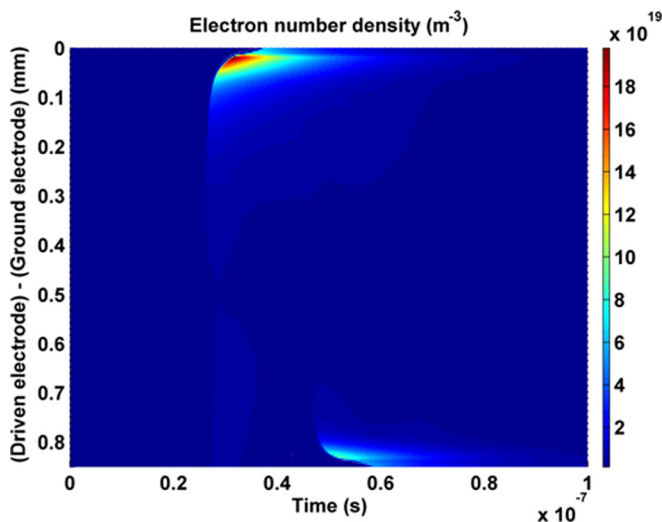
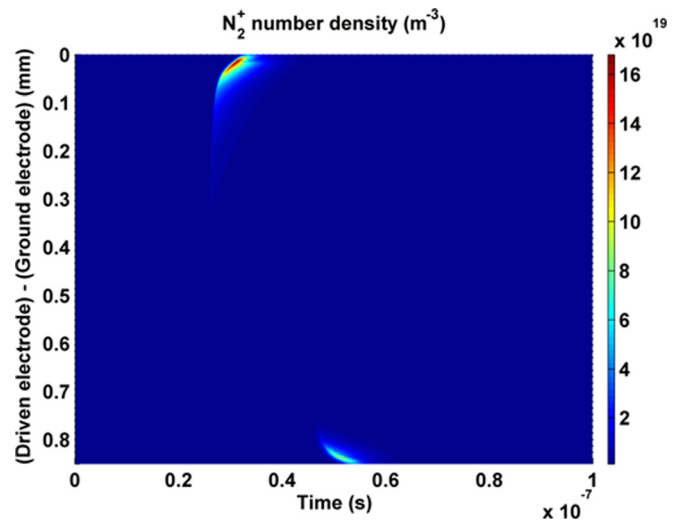


FIG. 4. Spatial-temporal distribution of the electron number density.

FIG. 5. Spatial-temporal distribution of N_2^+ .

propagates towards the grounded electrode. As the sheath thins such that the produced ions can reach the cathode surface, it strengthens further and is reduced further in thickness through a feedback mechanism as the ionization front provides more positive ions which in turn produce more secondary electrons which are accelerated through the sheath to sustain the ionization process. This increase in sheath strength and ionization is limited mostly by the temporally short voltage pulse as well as the accumulation of electrons and ions on the dielectric barrier surfaces. As the applied potential decreases, the sheath strength and ionization process also diminishes. Interestingly, when the applied potential decreases below approximately 1.55 kV, the potential across the discharge gap reverses (see Fig. 2(b) at 33 ns) due to the accumulated charge on the dielectric barrier surfaces. The dielectric barrier surface over the grounded electrode becomes more positively charged as the sheath adjacent to it collapses due to the ion-induced secondary electron emission. As the applied potential eventually reverses, the positively charged dielectric surface on the grounded electrode is rapidly neutralized by the high electron density in its vicinity (see Fig. 2(b) from 37 ns to 41.5 ns) and eventually charges negatively. The opposing dielectric barrier surface neutralizes by the immediate expelling of the accumulated electrons and/or negative ions on its surface. The driven electrode (which served as an anode for the initial positive voltage pulse) now becomes a cathode, and a sheath now begins to form adjacent to its dielectric surface (see Figs. 3 and 4 from 49 ns to 56 ns); however, the strength of the sheath and ionization during this reverse pulse is weaker because of the significantly weaker potential difference across the gap as a result of the faster charge accumulation at the dielectric surfaces associated with the generated electrons from the initial pulse.

The spatial-temporal distributions of N_2^+ , O_2^+ , and O_2^- number densities are shown in Figs. 5–7, respectively. A strong production of both N_2^+ and O_2^+ occurs concomitantly with the production of electrons, i.e., close to the grounded electrode when the applied potential is positive, and a weaker production close to the driven electrode when the

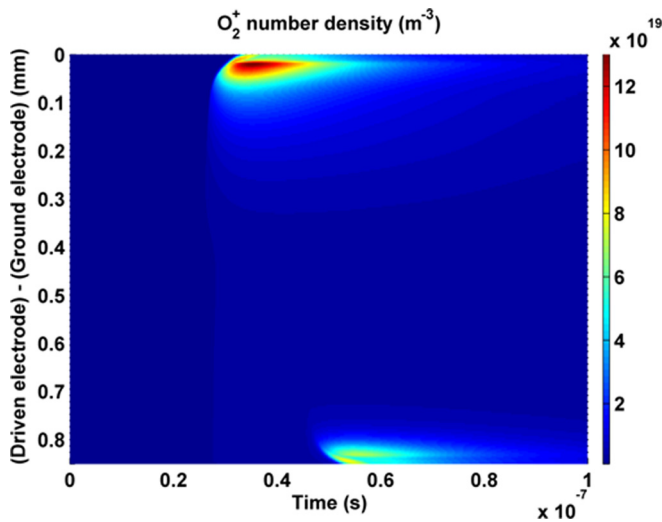
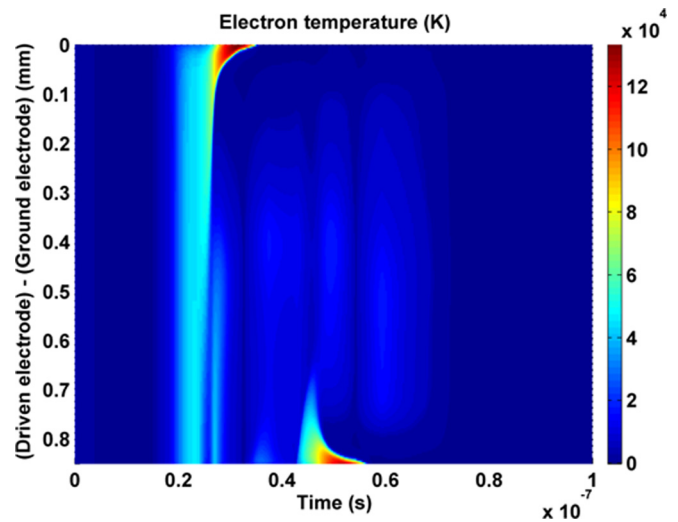
FIG. 6. Spatial-temporal distribution of O_2^+ .

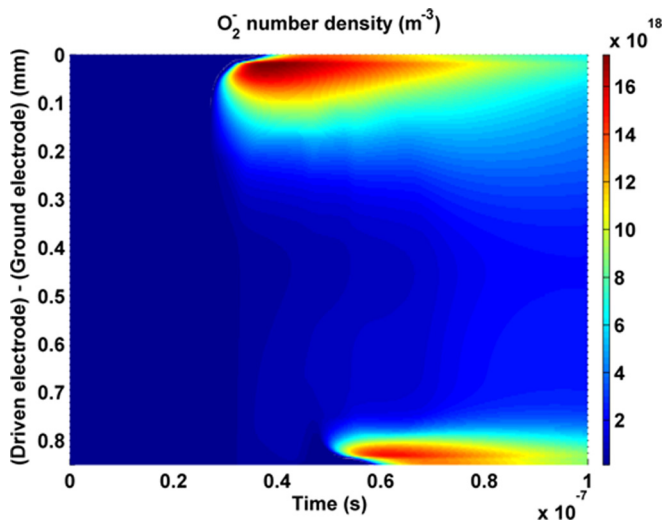
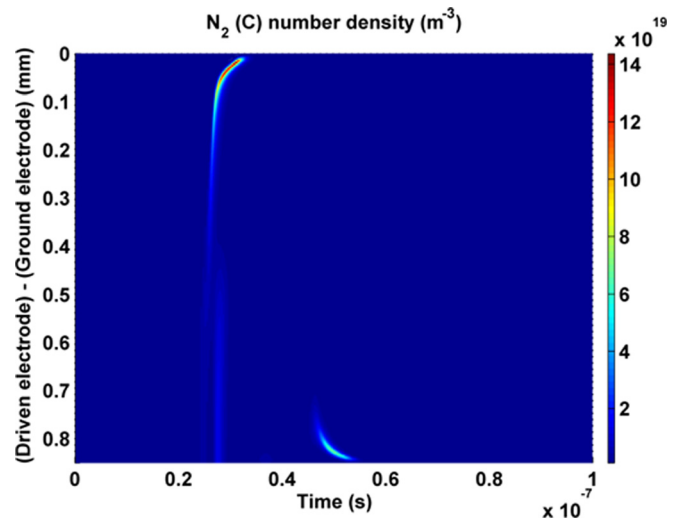
FIG. 8. Spatial-temporal distribution of electron temperature.

applied potential reverses. The N_2^+ density seems to decay much faster than that of O_2^+ , as a result of the fast ion conversion between N_2^+ and O_2 . A strong production of O_2^- also occurs in the strong ionization regions (close to the barrier surfaces) but later in time relative to the production of electrons and positive ions, as expected since O_2^- occurs primarily as a result of electron attachment. The electron attachment to O_2 is faster than the detachment process when the reduced electric field is less than approximately 120 Td based on the rate coefficients taken from the literature.^{24,25}

The spatial-temporal distribution of electron temperature is shown in Fig. 8. It is very similar to the electric field map because the electrons gain energy by Joule heating while they lose energy primarily through inelastic collisions resulting in excitations in energy states. Near the electrodes, the electron temperature exceeds 10 eV, but remains below about 4 eV in the bulk of the discharge.

The spatial-temporal distribution of the electronically excited N_2 (C) state is shown in Fig. 9. Its map is presented for comparison to the experimental results of Ref. 14, because the significant portion of the visible radiation from the

discharge in air is associated with the N_2 C-B electronic transition⁶⁻⁸ and is directly proportional to the N_2 (C) state density. In determining the N_2 (C) state density, we consider electron-impact excitation as well as collisional and radiation quenching processes, but do not include any pooling reactions by collisions between excited electronic state species. Since the excitation energy of this state is above 11.03 eV, relatively close to the ionization energy, the N_2 (C) state density map is qualitatively similar to the electron density map (Fig. 4). We see that the expected N_2 C-B emission will appear around the times when the positive and negative voltage pulses reach their peak values (around 26.5 ns and 50 ns). The emission first appears and is relatively strong in the sheath edge adjacent to the grounded electrode (initially a cathode), and then near the driven electrode region (which eventually becomes a cathode). The simulated emission map is in general qualitative agreement with that measured in Ref. 14 with quantitative registration in the onset of emission. We attribute the lack of broader quantitative agreement to uncertainties in kinetic rate constants, transport coefficients, as well as in the assumed secondary emission processes.

FIG. 7. Spatial-temporal distribution of O_2^- .FIG. 9. Spatial-temporal distribution of N_2 (C).

We compare our simulations of electric field and total discharge current density to the experimental results of Ref. 14 in Fig. 10. The experiments record the time-variation in the electric field at the center of the discharge using electric-field induced coherent Raman scattering (E-CRS) and the total current density. The experimental results reveal that the measured mid-gap electric field reaches half of its peak nominal electric field and then falls slightly before the nominal field decays. The experimental total current density is found to peak when the applied potential is at its most positive and negative values, reaching a level of about $8 \times 10^4 \text{ A/m}^2$. The corresponding results of the simulations for the mid-gap electric field and current densities and the comparisons to the results of Ref. 14 are shown in Figs. 10(a) and 10(b), respectively. The simulated mid-gap electric field is found to be slightly greater (about 2.5 times) than that measured. Despite this difference, it is noteworthy that the simulations capture the same general temporal features in the mid-gap electric field, including the decay of the mid-gap electric field earlier

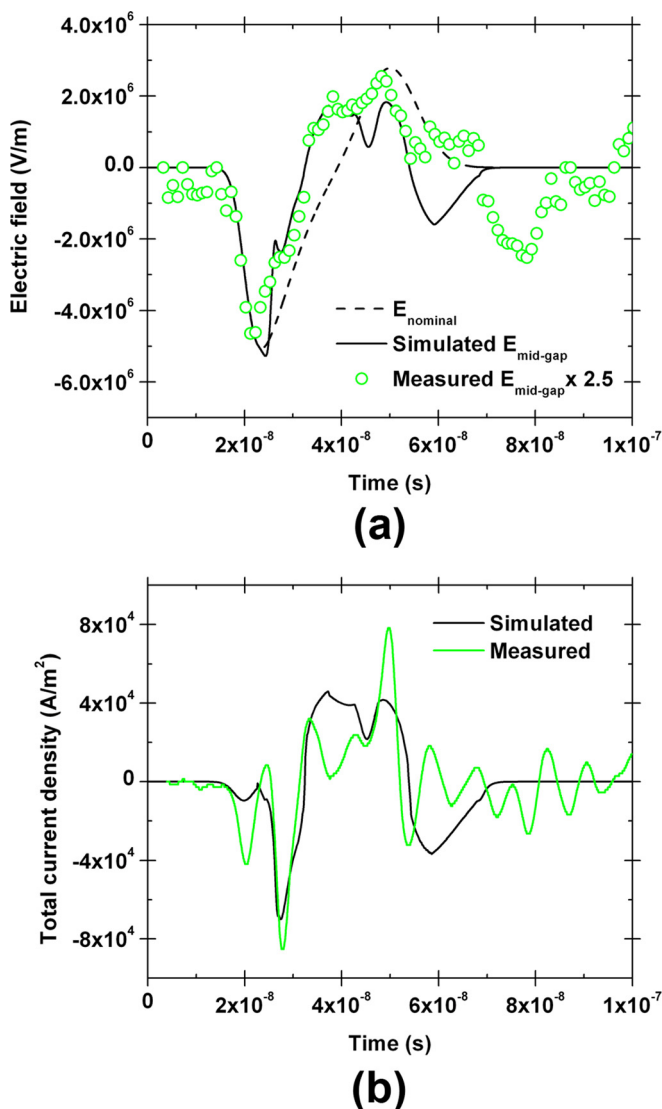


FIG. 10. (a) A comparison of the simulated electric field to that measured by Ito *et al.*¹⁴ (which is multiplied by a factor of 2.5 for the comparison). Also shown is the nominal electric field. (b) Simulated total current density compared to that measured in Ref. 14.

in time than the nominal field. This earlier decay of the electric field is due to the charge accumulation on the dielectric barrier surfaces associated with the rapid ionization within the sheath of the grounded electrode just prior to its collapse (see the dielectric barrier surface potentials in Fig. 2(b)). The larger predicted electric field might be attributed to the finite experimental resolution associated with the laser beam cross section (not reported in Ref. 14) and also, perhaps, the finite temporal resolution (3–5 ns FWHM). Other differences can be attributed to the experimental uncertainties in dielectric barrier thickness (and properties) and gap spacing.

IV. CONCLUSION

A nanosecond-pulsed dielectric barrier discharge in 340 K atmospheric pressure air was simulated under conditions similar to a recently reported experimental study in which mid-gap electric fields were measured.¹⁴ The simulations confirm what is measured experimentally, in that the mid-gap field initially tracks the nominal field expected since the positive and negative ions lingering from the previous discharge pulse are relatively immobile and cannot respond to the applied potential in the time scales of the voltage pulse. As the voltage pulse increases further, electrons bound to the molecular oxygen detach, are heated by the field, and incipient ionization takes place, first near the positively biased electrode. The ionization front is found to propagate from the positively biased driven electrode towards the grounded electrode (Meek's condition) much like the propagation of a streamer. This leads to the formation of a strong sheath close to the dielectric barrier adjacent to the grounded electrode. The increase in sheath strength is limited by the temporally short voltage pulse and the charge accumulation on the dielectric barrier surfaces. The sheath eventually collapses as a result of the secondary electron emission generated by the increasing positive ion bombardment of the dielectric barrier surface. Despite the bipolar nature of the voltage pulse simulated, an interesting feature of this DBD configuration is that the polarity of the discharge between the dielectric barrier surfaces reverses well before the reversal in the actual voltage pulse, due to the charge accumulation. As the voltage pulse eventually reverses in its polarity, a sheath then begins to form on the driven electrode, the strength of which is significantly weaker because of the lower applied potential and the faster charge accumulation on the dielectric surfaces as a result of the increased electron and ion densities.

ACKNOWLEDGMENTS

This work is supported by the National Science Foundation and the Department of Energy through the NSF/DOE Partnership in Basic Plasma Science. Partial support for M. S. Bak is provided through a Stanford Graduate Fellowship.

¹C. H. Kruger, C. O. Laux, L. Yu, D. M. Packan, and L. Pierrot, *Pure Appl. Chem.* **74**, 337–347 (2002).

²G. Pilla, D. Galley, D. A. Lacoste, F. Lacas, D. Veynante, and C. O. Laux, *IEEE Trans. Plasma Sci.* **34**, 2471–2477 (2006).

- ³M. S. Bak, H. Do, M. G. Mungal, and M. A. Cappelli, *Combust. Flame* **159**, 3128–3137 (2012).
- ⁴A. Yu. Starikovskii, A. A. Nikipelov, M. M. Nudnova, and D. V. Roupassov, *Plasma Sources Sci. Technol.* **18**, 034015 (2009).
- ⁵K. Takashima (Udagawa), Y. Zuzeek, W. R. Lempert, and I. V. Adamovich, *Plasma Sources Sci. Technol.* **20**, 055009 (2011).
- ⁶D. Z. Pai, G. D. Stancu, D. A. Lacoste, and C. O. Laux, *Plasma Sources Sci. Technol.* **18**, 045030 (2009).
- ⁷D. Z. Pai, D. A. Lacoste, and C. O. Laux, *Plasma Sources Sci. Technol.* **19**, 065015 (2010).
- ⁸M. S. Bak, W. Kim, and M. A. Cappelli, *Appl. Phys. Lett.* **98**, 011502 (2011).
- ⁹S. O. Macheret, M. N. Shneider, and R. B. Miles, *IEEE Trans. Plasma Sci.* **30**, 1301–1314 (2002).
- ¹⁰I. V. Adamovich, M. Nishihara, I. Choi, M. Uddi, and W. R. Lempert, *Phys. Plasmas* **16**, 113505 (2009).
- ¹¹J. Poggie, I. Adamovich, N. Bisek, and M. Nishihara, *Plasma Sources Sci. Technol.* **22**, 015001 (2013).
- ¹²A. V. Likhanskii, M. N. Shneider, S. O. Macheret, and R. B. Miles, *Phys. Plasmas* **14**, 073501 (2007).
- ¹³T. Unfer and J. P. Boeuf, *J. Phys. D: Appl. Phys.* **42**, 194017 (2009).
- ¹⁴T. Ito, T. Kanazawa, and S. Hamaguchi, *Phys. Rev. Lett.* **107**, 065002 (2011).
- ¹⁵A. V. Phelps and L. C. Pitchford, see <http://www.lxcat.laplace.univ-tlse.fr> for database (retrieved January 6, 2013).
- ¹⁶A. V. Phelps, see <http://www.lxcat.laplace.univ-tlse.fr> for database (retrieved January 6, 2013).
- ¹⁷Yu. P. Raizer, *Gas Discharge Physics* (Springer-Verlag, Berlin, Germany, 1991), Chaps. 5 and 14.
- ¹⁸G. J. M. Hagelaar and L. C. Pitchford, *Plasma Sources Sci. Technol.* **14**, 722–733 (2005).
- ¹⁹S. McGowan, *Can. J. Phys.* **45**, 439–448 (1967).
- ²⁰D. L. Scharfetter and H. K. Gummel, *IEEE Trans. Electron Devices* **16**, 64–77 (1969).
- ²¹A. C. Hindmarsh, P. N. Brown, K. E. Grant, S. L. Lee, R. Serban, D. E. Shumaker, and C. S. Woodward, *ACM Trans. Math. Softw.* **31**, 363–396 (2005).
- ²²See <http://www.netlib.org/lapack/> for the linear algebra package.
- ²³J. M. Meek, *Phys. Rev.* **57**, 722–728 (1940).
- ²⁴A. Kh. Mnatsakanyan and G. V. Naidis, *Reviews of Plasma Chemistry*, edited by B. M. Smirnov (Consultants Bureau, New York, 1991), Vol. 1, p. 259.
- ²⁵I. A. Kossyi, A. Yu. Kostinsky, A. A. Matveyev, and V. P. Silakov, *Plasma Sources Sci. Technol.* **1**, 207–220 (1992).
- ²⁶M. Capitelli, C. M. Ferreira, B. F. Gordiets, and A. I. Osipov, *Plasma Kinetics in Atmospheric Gases* (Springer, Berlin, 2000).